A Two-in-One Strategy to Simultaneously Boost the Site Density and Turnover Frequency of Fe−N−C Oxygen Reduction Catalysts

Jianbin Liu[+], *Yao Liu*[+], *Bing Nan*[+], *Dashuai Wang, Christopher Allen, Zhichao Gong, Guanchao He, Kaixing Fu, Gonglan Ye, Huilong Fei*[*]

J. Liu, Z. Gong, G. He, Prof. G. Ye, Prof. H. Fei
State Key Laboratory for Chemo/Biosensing and Chemometrics, Advanced Catalytic Engineering Research Center of the Ministry of Education and College of Chemistry and Chemical Engineering, Hunan University, Changsha 410082, P. R. China.

Y. Liu, Dr. D. Wang
Institute of Zhejiang University—Qu Zhou, Qu Zhou 324000, China.

Dr. B. Nan
Shanghai Synchrotron Radiation Facility, Shanghai Advanced Research Institute, Chinese Academy of Sciences, Shanghai 201210, China.

Dr. C. Allen
Department of Materials, University of Oxford, Parks Road, Oxford OX1 3PH, UK, and Electron Physical Science Imaging Centre, Diamond Light Source Ltd., OX11 0DE, UK.

Dr. K. Fu
School of Environmental Science and Engineering, Shanghai Jiao Tong University, Shanghai 200240, China

[+] These authors contributed equally to this work.
* Correspondence: hlfei@hnu.edu.cn

Abstract

Site density (SD) and turnover frequency (TOF) are the two fundamental kinetic descriptors that determine the oxygen reduction activity of iron-nitrogen-carbon (Fe−N−C) catalysts that represent the most promising alternatives to precious and scarce platinum. However, it remains a grand challenge to simultaneously optimize these two parameters in a single Fe−N−C catalyst. Here we show that treating a typical Fe−N−C catalyst with ammonium iodine (NH_4I) vapor via a one-step chemical vapor deposition process not only increases the surface area and porosity of the catalyst (and thus enhanced exposure of active sites) via the etching effect of the in-situ released NH_3, but also regulates the electronic structure of the Fe−N_4 moieties by the iodine dopants incorporated into the carbon matrix. As a result, the NH_4I-treated Fe−N−C catalyst possesses both high values in the SD of 2.15×10^{19} sites g^{-1} (×2 enhancement compared to the untreated counterpart) and TOF of 3.71 electrons $site^{-1}$ s^{-1} (×3 enhancement) that correspond to a high mass activity of 12.78 A g^{-1}, as determined by in-situ nitrite stripping technique. Moreover, this catalyst exhibits an excellent oxygen reduction activity in base with a half-wave potential ($E_{1/2}$) of 0.924 V and acceptable activity in acid with $E_{1/2}$ = 0.795 V, and superior power density of 249.1 mW cm^{-2} in a zinc-air battery.

Introduction

Electrochemical energy conversion devices such as fuel cells and metal-air batteries play critical roles in addressing the global environmental and energy crisis.[1-4] The oxygen reduction reaction (ORR) occurring at the cathode of these devices requires the use of platinum (Pt)-based catalysts to promote its sluggish kinetics. However, the high cost and scarcity of Pt precludes its widespread deployment, thus calling for the development of Pt-group metal-free (PGM-free) catalysts with comparable or even superior catalytic activity.[5, 6] Among Pt-free candidates, iron-nitrogen-carbon (Fe−N−C) catalysts, with atomically dispersed Fe−N_4 active sites embedded in the carbon matrix, are most promising for their encouraging ORR activity in both acidic and alkaline electrolytes.[7-10]

Fe−N−C catalysts are commonly synthesized by the pyrolysis of iron-, nitrogen- and carbon-containing precursors and their ORR activity has been dramatically improved over the past decades by varying the precursor combinations and/or pyrolysis conditions.[11, 12] Nevertheless, the current understanding of the correlation between the synthesis and experimentally observed catalytic activity has remained somewhat elusive and empirical, precluding the rational improvement in the ORR activity of Fe−N−C catalysts.[13, 14] Fortunately, this issue has been largely resolved since effective methods (i.e., adsorption/desorption techniques with CO or NO as the probe molecules) became available to identify and quantify the Fe sites located at the surface of Fe−N−C catalysts, which enables the deconvolution of the overall activity of mass specific current density (j_m) into the per-site intrinsic activity of turnover

frequency (TOF) and site density (SD), according to: j_m [A g^{-1}] = SD [sites g^{-1}] × TOF [electron $site^{-1}$ s^{-1}] × e [C $electron^{-1}$].[15-17] As such, TOF and SD are considered the two fundamental descriptors of the kinetic reactivity of Fe−N−C catalysts and can provide catalyst synthesis guidelines for performance improvements.

Based on the above equation, synthetic approaches to increasing either the TOF value or the SD value could result in the improvement in the overall activity of Fe−N−C catalysts. For the intrinsic TOF, it is dictated by the electronic structure of the Fe sites that determines the adsorption strength of oxygen intermediates. Accordingly, enhancements in the TOF value have been achieved by various electronic structure tuning strategies, among which heteroatoms (e.g., O, S, B and P) are most frequently adopted to modulate the Fe coordination environments either in the first coordination sphere or the outer coordination spheres.[18-20] As for the SD, it is affected by both the content of the atomically dispersed Fe and the utilization efficiency of the Fe−N_4 active sites.[21, 22] To increase the SD value, a variety of modifications in the pyrolysis synthesis were introduced.[23-25] Notable examples include the exchanging of Fe into a preformed Zn−N−C matrix to achieve high Fe loadings, and introducing silica coating into the pyrolysis precursors to enhance the accessibility of the Fe−N_4 sites by improving the porosity and surface area of the Fe−N−C catalyst.[26, 27] However, the majority of existing strategies to develop more active Fe−N−C catalysts focus solely on either the TOF or the SD; worse still, there were cases when trade-offs had to be made, i.e., the increase in the TOF was achieved at the sacrifice of the SD or vice versa.[26] For example, the switch from polyaniline to

zeolitic imidazole framework (ZIF) as the C/N precursors for synthesizing Fe−N−C catalysts led to ~ 3 times enhancement in the TOF, which however was offset by the lowering in the SD to the similar extent, thus resulting in negligible improvement in the overall activity.[15] To overcome this dilemma, it is imperative to explore new strategies to optimize TOF and SD of Fe−N−C catalysts in a concerted manner.

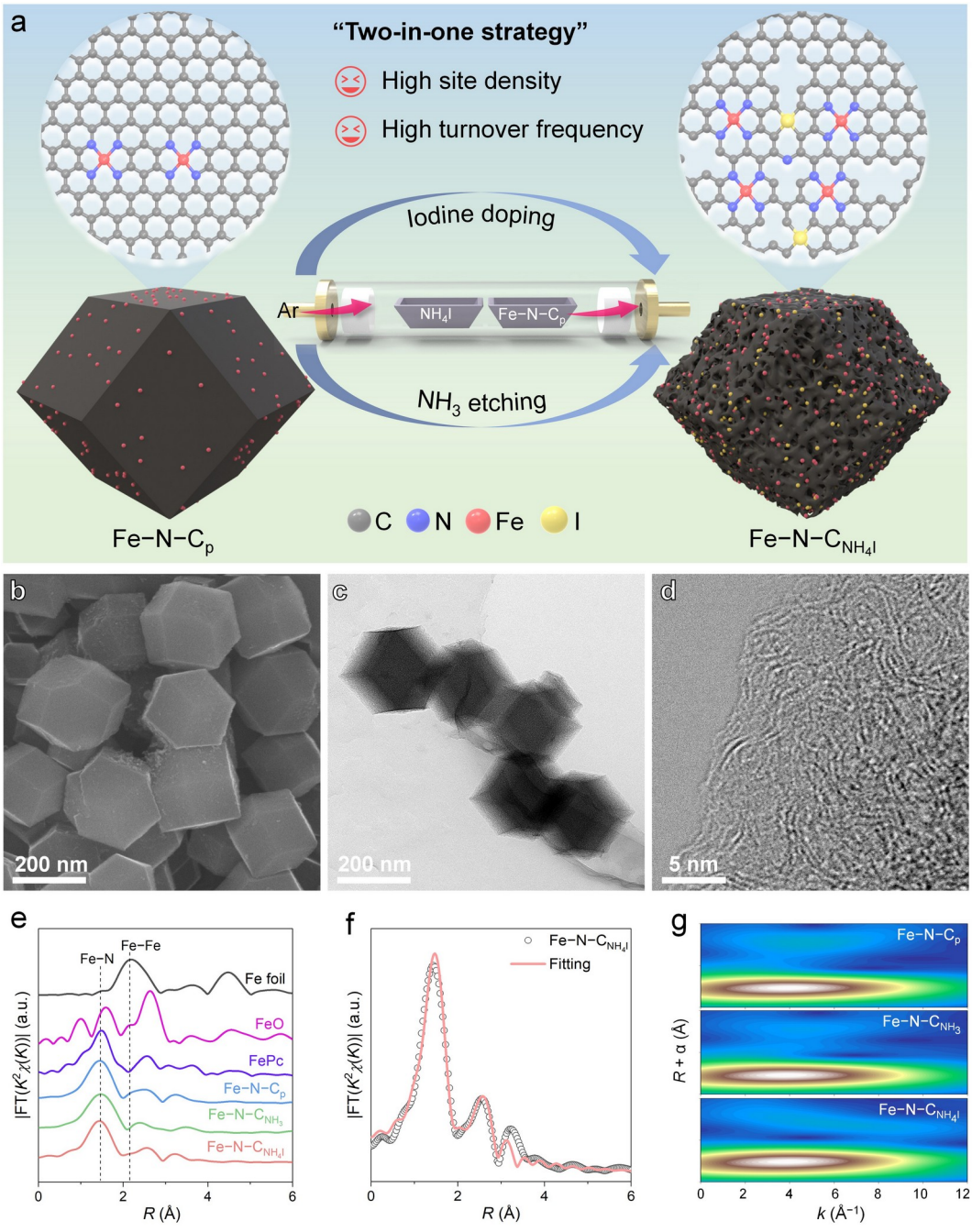

Figure 1. Synthesis and characterizations of Fe−N−C_{NH4I}. (a) Schematic illustration of the "two-in-one strategy" for boosting the TOF and SD values of Fe−N−C via a one-step NH_4I treatment. (b) SEM image, (c) low-magnification TEM image, and (d) high-magnification TEM image of Fe−N−C_{NH4I}. (e) The FT-EXAFS spectra for Fe−N−C_p, Fe−N−C_{NH3} and Fe−N−C_{NH4I}, along with reference samples of Fe foil, FeO and FePc. (f) EXAFS fitting curve at *R* space for Fe−N−C_{NH4I}. (g) Fe *K*-edge EXAFS-WT contour plots of Fe−N−C_p, Fe−N−C_{NH3} and Fe−N−C_{NH4I}.

Herein, we developed an Fe−N−C catalyst that simultaneously achieved high SD and TOF values through a one-step treatment of a pristine Fe−N−C material with ammonium iodine (NH_4I) vapor in a facile chemical vapor deposition process. The high-temperature NH_4I treatment not only increased the surface area (from 801.4 m^2 g^{-1} to 1413.7 m^2 g^{-1}) by producing abundant defects and pores in the carbon substrate, but also optimally modified the electronic structure of the Fe sites by incorporating the iodine (I) atom dopants into the carbon matrix (Figure 1a). In-situ nitrite stripping quantified that the NH_4I-treated Fe−N−C catalyst (denoted as Fe−N−C_{NH4I}) has a SD value of 2.15×10^{19} sites g^{-1} paired with a TOF value of 3.71 electrons $site^{-1}$ s^{-1},

resulting in a high mass activity with j_m = 12.78 A g^{-1}. Notably, the SD and TOF values of this catalyst are ~ 2 times and ~ 3 times, respectively, higher than those of the untreated counterpart. Multiple experimental characterizations combined with density functional theory calculations reveal that the I dopants could regulate the *d*-band center of the catalyst to offer optimal adsorption strength of the oxygen intermediates and thus promote the ORR process. Together, Fe−N−C_{NH4I} exhibited an excellent ORR activity in base in a rotating ring disk electrode (RRDE) and Zn-air battery measurements, along with acceptable activity in acid.

Results and Discussion

Catalyst synthesis and characterizations. The preparation steps of Fe−N−C_{NH4I} were schematically illustrated in Figure S1. Briefly, a pristine Fe−N−C material (denoted as Fe−N−C_p) was firstly prepared by carbonizing Fe-doped ZIF-8 nanocrystals at 1000 °C for 2 h under Ar atmosphere, which has now become a standard and most popular protocol to prepare Fe−N−C catalysts.[28-30] Then, Fe−N−C_p and NH_4I powder were placed in two separate porcelain boats with NH_4I in the upstream of the quartz tube furnace and secondary pyrolysis was performed at 850 °C for 1 h under Ar atmosphere to obtain the final product of Fe−N−C_{NH4I}. To highlight the importance of I dopants in modifying the electronic structure and catalytic activity of Fe−N−C_{NH4I}, a control sample was prepared following the similar procedures

except that NH_4I was removed during the second-step pyrolysis and the gaseous atmosphere was switched from Ar to Ar/NH_3. The resultant control catalyst is denoted as Fe−N−C_{NH3}.

From scanning electron microscopy (SEM) and low-magnification transmission electron microscopy (TEM) characterizations (Figure 1b,c and Figure S2), Fe−N−C_{NH4I}, Fe−N−C_{NH3} and Fe−N−C_p all present a truncated polyhedron shape with the particle size in the range of 200 − 300 nm, similar to the non-pyrolyzed ZIF-8 precursor. Additionally, no Fe-derived metal clusters or nanoparticles were observed. The absence of metal crystallites was confirmed by the X-ray diffraction patterns (Figure S3). High-magnification TEM images display the disordered carbon layers with randomly oriented graphitic domains in these three catalysts (Figure 1d and Figure S4).[31] The existent form of the Fe metals was investigated by extended X-ray absorption fine structure (EXAFS) analysis at the Fe *K*-edge. Figure 1e shows the EXAFS Fourier transform (FT-EXAFS) of Fe−N−C_{NH4I}, Fe−N−C_{NH3} and Fe−N−C_p, along with the reference samples of Fe foil, FeO and iron phthalocyanine (FePc). Similar to FePc, Fe−N−C_{NH4I}, Fe−N−C_{NH3} and Fe−N−C_p all present a major peak at ~ 1.46 Å, which is much shorter than the Fe−O peak at 1.59 Å for the FeO_6 octahedra in FeO and therefore can be assigned to the backscattering between Fe and light atoms.

[32] The minor peak at ~2.5 Å could be attributed to the scattering path of Fe−C in the second coordination sphere of the Fe site.[33, 34] In addition, the Fe−Fe bond at 2.14 Å in Fe foil was absent in the three catalysts, excluding the existence of metallic Fe crystallites. Quantitative least-squares EXAFS curve-fitting analysis in *R* and *k* space determines that the coordination numbers of the Fe−N path in Fe−N−C_{NH4I}, Fe−N−C_{NH3} and Fe−N−C_p are all close to 4.0, suggesting the adoption of the Fe−N_4 coordination configuration (Figure 1f, Figure S5 and Table S1). EXAFS wavelet transform (EXAFS-WT) analysis, which can discriminate the backscattering atoms even when they overlap substantially in *R*-space by providing not only radial distance resolution but also *k*-space resolution, confirms the atomic dispersion of the Fe in the three catalysts as the spectra detects only one intensity maximum at ~ 4.0 $Å^{-1}$ in *k* space that can be ascribed to the Fe−N contributions (Figure 1g), and no spectral features ascribed to possible Fe-I bonding were observed.[35]

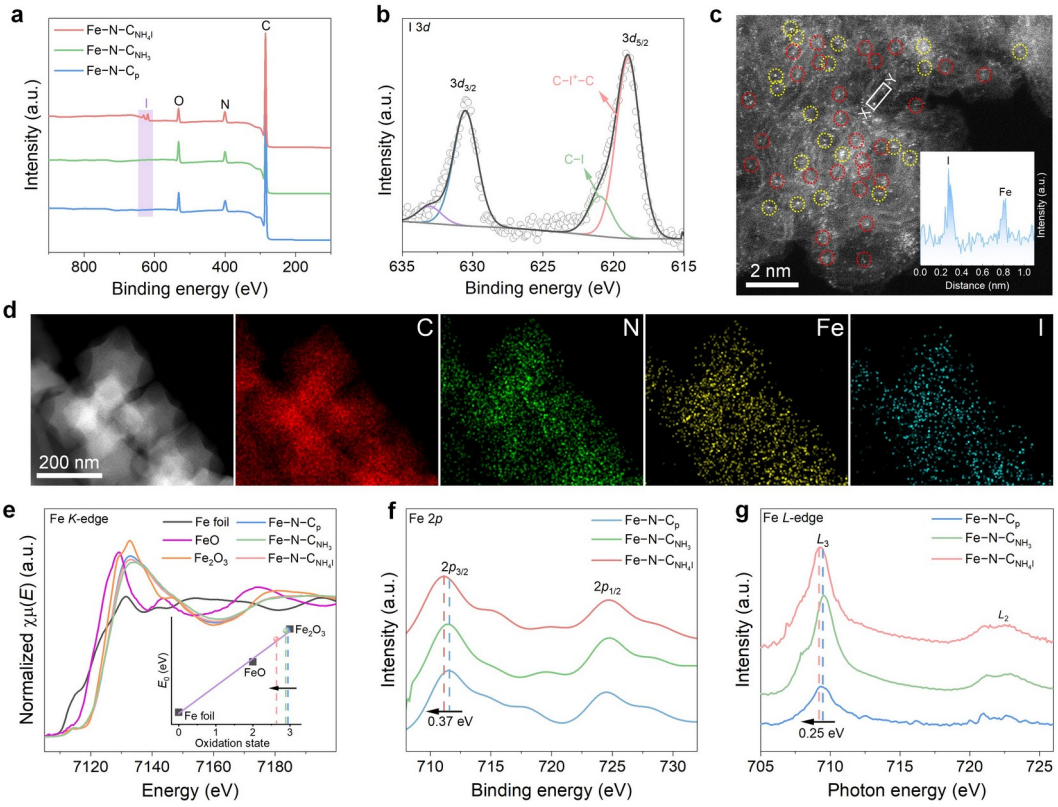

Figure 2. NH_4I treatment-induced changes in composition and electronic structure. (a) XPS survey spectra of Fe−N−C_p, Fe−N−C_{NH3} and Fe−N−C_{NH4I}. (b) High-resolution XPS I 3*d* spectra of Fe−N−C_{NH4I}. (c) HAADF-STEM image of Fe−N−C_{NH4I}. The Fe atoms and I atoms with different *Z* contrasts are marked by red and yellow circles, respectively. The inset shows the intensity profiles along *X*−*Y* in the image. (d) EDS elemental maps of C, N, Fe and I in Fe−N−C_{NH4I}. (e) Fe *K*-edge XANES spectra of Fe−N−C_p, Fe−N−C_{NH3}, Fe−N−C_{NH4I} and the reference samples. The inset shows the fitted average oxidation states of Fe derived from the XANES spectra. (f) High-

resolution XPS Fe 2*p* spectra of Fe−N−C_p, Fe−N−C_{NH3} and Fe−N−C_{NH4I}. (g) XANES spectra at the Fe *L*-edge of Fe−N−C_p, Fe−N−C_{NH3} and Fe−N−C_{NH4I}.

NH_4I treatment-induced compositional and structural changes. The compositions of the catalysts were probed by X-ray photoelectron spectroscopy (XPS). XPS survey spectra reveal the obvious presence of C, N and O elements in Fe−N−C_{NH4I}, Fe−N−C_{NH3} and Fe−N−C_p, while an additional peak ascribed to the I element (0.14 at %) was clearly observed in Fe−N−C_{NH4I} (Figure 2a and Figure S6). From the high-resolution XPS I 3*d* spectra of Fe−N−C_{NH4I}, the I $3d_{5/2}$ peak can be deconvoluted into two peaks at ~ 618.9 and ~ 620.8 eV that can be assigned to the ionic C−I^+−C and covalent C−I species, respectively (Figure 2b).[36] The peak for Fe in the XPS survey spectra for all three catalysts was negligible due to its low content. The Fe contents were determined to be similar for Fe−N−C_{NH4I} (1.85 wt%), Fe−N−C_{NH3} (1.97 wt%) and Fe−N−C_p (1.47 wt%) by inductively coupled plasma mass spectrometry (ICP-MS). The metal contents in these catalysts are comparable to those in previously reported Fe−N−C catalysts (Table S2). The high-resolution XPS N 1*s* spectra were

displayed in Figure S7 and four types of N species were identified, namely pyridinic N (~ 398.7 eV), pyrrolic N (~ 400.1 eV), graphitic N (~ 401.2 eV) and N-oxide (~ 402.8 eV). High-angle annular dark-field scanning transmission electron microscopy (HAADF-STEM) reveals the presence of two sets (highlighted by red and yellow circles) of evenly dispersed bright dots with different intensities, which were identified to be Fe atoms and I atoms, respectively, via the *Z*-contrast analysis (Figure 2c).[36] STEM energy-dispersive X-ray spectrometry (EDS) elemental mapping shows the uniform distribution of C, N, Fe and I elements throughout the sample of Fe−N−C_{NH4I} (Figure 2d). The uniform distribution of the atomic Fe sites and different elements in Fe−N−C_p and Fe−N−C_{NH3} were observed in the corresponding HAADF-STEM images and EDS elemental mappings (Figure S8). To further clarify the existent form of I species in Fe−N−C_{NH4I}, the I L_3-edge X-ray absorption near-edge structure (XANES) spectra and FT-EXAFS spectra of Fe−N−C_{NH4I}, along with iohexol containing I−C bonds as reference, were analyzed (Figure S9). As shown in the XANES spectra (Figure S9b), Fe−N−C_{NH4I} and iohexol displayed similar absorption edges, suggesting the comparable coordination environment around the I

atoms. From the FT-EXAFS spectra (Figure S9c), similar to iohexol, Fe−N−C_{NH4I} exhibits a major peak at ~1.44 Å, which can be assigned to the I−C bonding in the first coordination shell, confirming the atomic dispersion of I elements and formation of I−C bonds.[37, 38] Figure 2e displays the Fe *K*-edge XANES spectra of the three catalysts, along with the reference samples of Fe foil, FeO and Fe_2O_3. The XANES profiles of Fe−N−C_{NH4I}, Fe−N−C_{NH3} and Fe−N−C_p are markedly different from those of the reference samples but are similar among themselves, suggesting their comparable bonding configurations of the Fe sites. The absorption edges of the three catalysts approached that of Fe_2O_3, indicating that the Fe oxidation state was close to +3. The first derivative curves of the Fe *K*-edge XANES spectra were utilized to identify the average Fe oxidation state that was correlated with the *K*-edge absorption position (Figure S10).[39] From the linear curve fitting obtained for Fe foil, FeO and Fe_2O_3 with different oxidation states, the Fe oxidation state of Fe−N−C_{NH4I} (+2.63) is lower than that of Fe−N−C_{NH3} (+2.89) and Fe−N−C_p (+2.93) (Figure 2e, inset). The reduced Fe oxidation state in Fe−N−C_{NH4I} was confirmed by the Fe 2*p* XPS and Fe *L*-edge XANES spectra (Figure 2f,g and Figure S11), where significant negative shifts in the peak positions were observed compared to Fe−N−C_{NH3} and Fe−N−C_p. Notably,

the comparable XPS and XANES peak positions and hence the Fe oxidation state between Fe−N−C_{NH3} and Fe−N−C_p highlight that the modulated electronic structure of Fe−N−C_{NH4I} is induced by the I dopants.

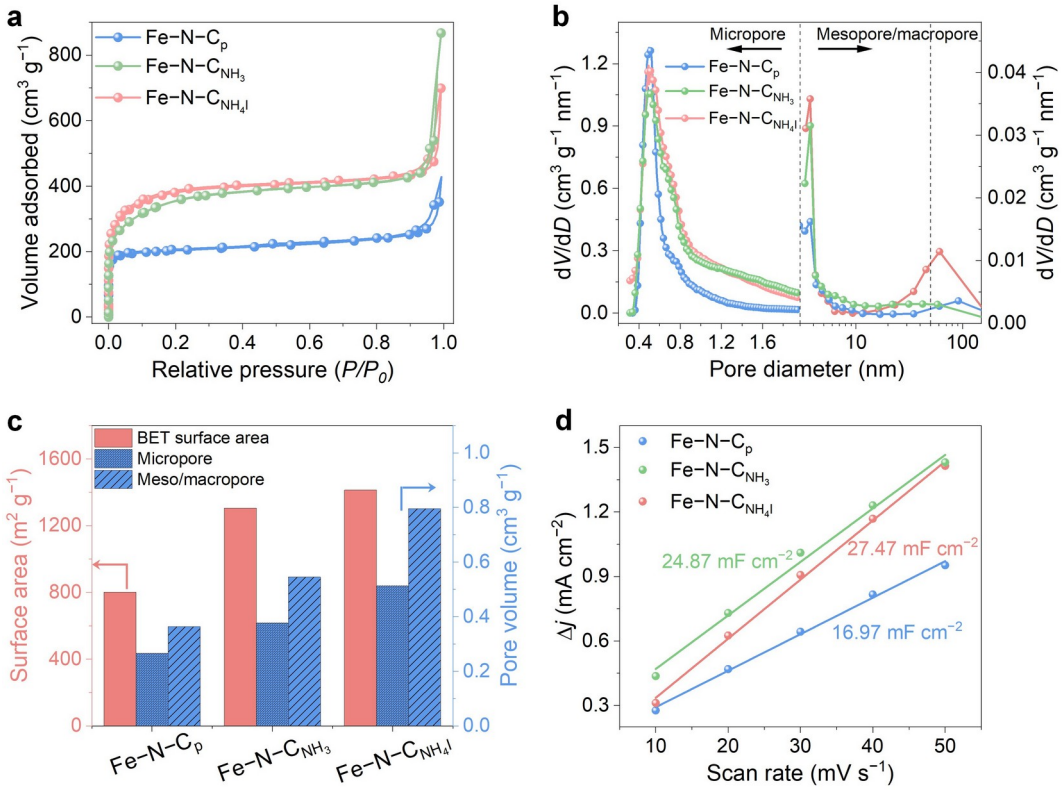

Figure 3. NH_4I treatment-induced changes in porous structures. (a) N_2 adsorption and desorption isotherms of Fe−N−C_p, Fe−N−C_{NH3} and Fe−N−C_{NH4I}. (b) The pore size distributions for Fe−N−C_p, Fe−N−C_{NH3} and Fe−N−C_{NH4I}. (c) Comparisons of the BET specific surface areas, micropore volume and meso/macropore volume of Fe−N−C_p,

Fe−N−C_{NH3} and Fe−N−C_{NH4I}. (d) The electrochemical double layer capacitance of Fe−N−C_p, Fe−N−C_{NH3} and Fe−N−C_{NH4I}.

Besides the I-doping induced electronic tuning effect, the high-temperature NH_4I treatment can additionally generate porous structure in Fe−N−C_{NH4I} by the etching effect of the in-situ released NH_3. The specific surface area and porosity of the catalysts were firstly investigated by N_2 sorption analysis (Figure 3a-c). All the three catalysts display the mixed type-Ⅰ and type-Ⅳ adsorption-desorption isotherms in the low relative pressure (P/P_0 < 0.1) and the high pressure (P/P_0 > 0.8) regions, indicating the characteristic of hierarchical porosity in the catalysts (Figure 3a).[40, 41] For Fe−N−C_p, it possesses a Brunauer-Emmett-Teller (BET) surface area of 801.4 m^2 g^{-1}. After being treated with NH_4I or NH_3, the surface areas of Fe−N−C_{NH4I} and Fe−N−C_{NH3} were significantly increased to 1413.7 m^2 g^{-1} and 1305.9 m^2 g^{-1}, respectively. Additionally, from the N_2 sorption isotherms of Fe−N−C_{NH4I} and Fe−N−C_{NH3}, there is a sharp increase in the adsorption capacity at low relative pressures (P/P_0 < 0.1), indicating that the increased surface area was mainly attributed

to the enrichment in micropores, which were generated by the high-temperature etching effects of NH_3 from either the decomposition of NH_4I or the NH_3 gas flow in the second-step pyrolysis during catalysts preparation.[42, 43] Besides, pore size distribution was analyzed using the Horvath-Kawazoe (HK) method for micropores (d < 2 nm) and the Harrett-Joyner-Halenda (BJH) for mesopores and macropores (2 < d < 100 nm).[44, 45] As shown in Figure 3b, Fe−N−C_{NH4I} and Fe−N−C_{NH3} exhibit more abundant micropores (centered at ~ 0.6 nm) and mesopores (centered at ~ 3.0 nm) compared to Fe−N−C_p. The micropore volume (V_{micro}) and meso/macropore volume ($V_{meso/macro}$) of the three catalysts were summarized in Figure 3c and Table S3. The results show that Fe−N−C_{NH4I} has V_{micro} = 0.513 $cm^3\ g^{-1}$ and $V_{meso/macro}$ = 0.796 $cm^3\ g^{-1}$, higher than those of Fe−N−C_{NH3} (V_{micro} = 0.377 $cm^3\ g^{-1}$, $V_{meso/macro}$ = 0.545 $cm^3\ g^{-1}$) and Fe−N−C_p (V_{micro} = 0.265 $cm^3\ g^{-1}$, $V_{meso/macro}$ = 0.364 $cm^3\ g^{-1}$). Raman spectra for the three catalysts exhibit two peaks at ~ 1359 cm^{-1} and ~ 1595 cm^{-1} that can be assigned to the disordered sp^3 carbon (D band) and graphitic sp^2 carbon (G band), respectively (Figure S12). The I_D-to-I_G ratios for Fe−N−C_{NH4I} (0.92) and Fe−N−C_{NH3} (0.91) were larger than that of Fe−N−C_p (0.87), suggesting the higher defective degree of the carbon matrix in them. Additionally, the electrochemically active surface area (ECSA) was estimated by measuring the double-layer capacitance (C_{dl}) in the non-Faradaic

potential range. The results show that the ECSA value of Fe−N−C_{NH4I} (134.6 cm^2) is notably higher than those of Fe−N−C_{NH3} (121.8 cm^2) and Fe−N−C_p (83.2 cm^2) (Figure 3d and Figure S13). The improved surface area and porosity, particularly meso/macropores of Fe−N−C_{NH4I}, are beneficial for exposing more active sites.

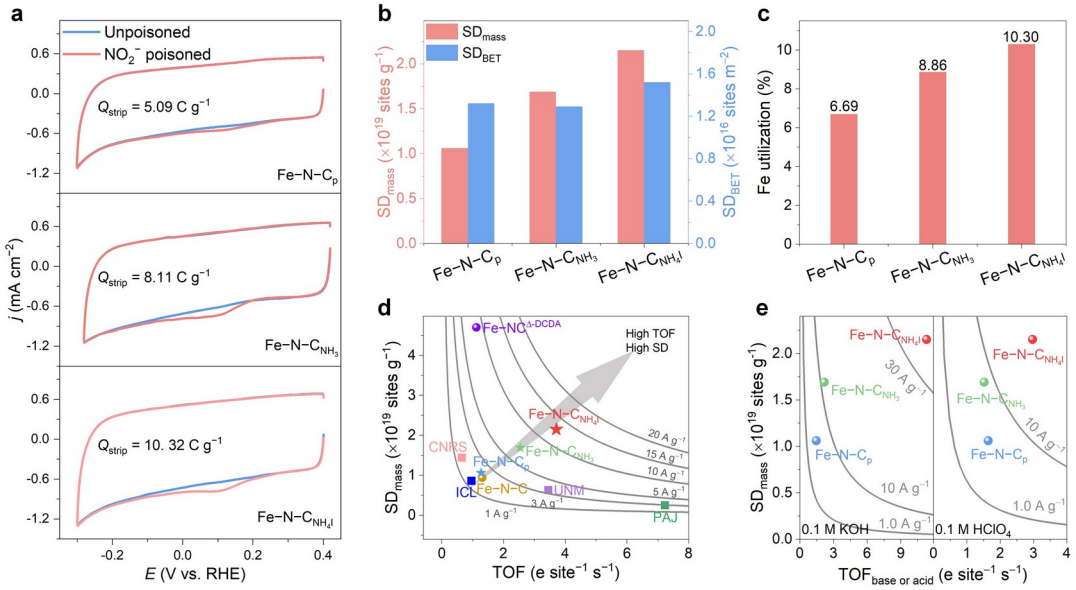

Figure 4. Analysis of SD and TOF. (a) Nitrite stripping voltammetry for Fe−N−C_p, Fe−N−C_{NH3} and Fe−N−C_{NH4I} in N_2-saturated 0.5 M acetate electrolyte buffer (pH = 5.2). (b) SD normalized by mass (SD_{mass}) and BET surface area (SD_{BET}). (c) Comparison of Fe utilization efficiency among Fe−N−C_p, Fe−N−C_{NH3} and

Fe−N−C_{NH4I}. (d) SD_{mass}-TOF maps with iso-mass activity curves at 0.80 V versus RHE in 0.5 M acetate buffer electrolyte (pH = 5.2) comparing the ORR activity metrics of Fe−N−C_p, Fe−N−C_{NH3} and Fe−N−C_{NH4I} developed in this work to recently reported benchmark Fe−N−C catalysts. (e) SD_{mass}-TOF maps with iso-mass activity curves at 0.90 V versus RHE in 0.1 M KOH and 0.80 V versus RHE in 0.1 M $HClO_4$ comparing the ORR activity of Fe−N−C_p, Fe−N−C_{NH3} and Fe−N−C_{NH4I}.

Analysis of SD and TOF. Some I-modified Fe−N−C catalysts have shown improved ORR performances,[46-49] but the SD and thus TOF values were not quantified, preventing the deconvolution of the overall activity and further the understanding of the origin for the enhanced apparent activity. In the present case, the SD values of Fe−N−C_{NH4I}, Fe−N−C_{NH3} and Fe−N−C_p were quantified by the in-situ electrochemical stripping of NO formed by exposure to nitrite (NO_2^-) in 0.5 M acetate buffer electrolyte (pH = 5.2) (Figure S14).[50] Well-defined reduction peaks resulting from the reduction of NO_2^- to form NO−Fe adduct were observed for the three catalysts in their poisoned cyclic voltammetry (CV) curves between − 0.30 V and 0.30 V versus reversible hydrogen electrode (RHE) (Figure 4a). The SD values can be estimated by the amounts of electric charge (Q_{strip}) needed to strip the adsorbed NO via the three-electron reduction process to form hydroxylamine.[22] The results show

that Fe−N−C_{NH4I} exhibited a Q_{strip} value of 10.32 C g^{-1} that is about two times that of Fe−N−C_p (Q_{strip} = 5.09 C g^{-1}) and notably higher than that of Fe−N−C_{NH3} (Q_{strip} = 8.11 C g^{-1}). The corresponding SD values normalized by mass (SD_{mass}) and BET surface area (SD_{BET}) were compiled in Figure 4b, displaying that the values for Fe−N−C_{NH4I} (SD_{mass}= 2.15×10^{19} sites g^{-1}, SD_{BET} = 1.52×10^{16} sites m^{-2}) are higher than Fe−N−C_{NH3} (SD_{mass}= 1.69×10^{19} sites g^{-1}, SD_{BET} = 1.29×10^{16} sites m^{-2}) and Fe−N−C_p (SD_{mass}= 1.06×10^{19} sites g^{-1}, SD_{BET} = 1.32×10^{16} sites m^{-2}). The Fe utilization efficiency factor (U_{Fe}), defined as the ratio of the number of electrochemically accessible Fe sites to the total Fe sites from the ICP-MS results, was evaluated.[22, 51] As shown in Figure 4c, Fe−N−C_{NH4I} possesses a U_{Fe} value of 10.30%, higher than those of Fe−N−C_{NH3} (U_{Fe} = 8.86%) and Fe−N−C_p (U_{Fe} = 6.69%), which can be ascribed to their differed surface area and porosity.

To compare the intrinsic ORR activity among the three catalysts, their TOF values were evaluated based on the above-determined SD_{mass} and the differential ORR kinetic current densities of the poisoned and the non-poisoned state of the catalysts at pH = 5.2. The TOF value of Fe−N−C_{NH4I} was determined to be 3.71 e $site^{-1}$ s^{-1} (at 0.8

V versus RHE), which is higher than those of Fe−N−C_{NH3} (2.54 e $site^{-1}$ s^{-1}) and Fe−N−C_p (1.27 e $site^{-1}$ s^{-1}). With SD and TOF values at hand, SD-TOF reactivity map can be created to analyze the catalytic ORR reactivity (Figure 4d). The four benchmark catalysts (CNRS, ICL, UNM and PAJ) and the recently reported catalyst of Fe−$NC^{\Delta\text{-DCDA}}$ were included in the reactivity map for comparison purpose.[17, 26] It can be seen that Fe−$NC^{\Delta\text{-DCDA}}$ has the highest SD_{mass} (4.7×10^{19} sites g^{-1}) but unsatisfactory TOF values (1.12 e $site^{-1}$ s^{-1}), while the PAJ catalyst has the highest TOF (7.23 e $site^{-1}$ s^{-1}) but disappointing SD_{mass} (0.25×10^{19} sites g^{-1}). In comparison, our Fe−N−C_{NH4I} catalyst combines both high SD_{mass} and TOF values, which together leads to a mass activity (j_m = 12.78 A g^{-1}) higher than Fe-$NC^{\Delta\text{-DCDA}}$ (j_m = 8.43 A g^{-1}), PAJ (j_m = 2.89 A g^{-1}) and other benchmark catalysts. Considering that Fe−N−C_{NH4I} performed excellently in alkaline and acid electrolytes (discussed later), we established alternative SD-TOF maps of the catalysts in acid and base by combining the SD from the NO_2^- stripping measurements and the ORR kinetic current densities determined in 0.1 M KOH and 0.1 M $HClO_4$, respectively (Figure 4e). The as-determined TOFs in base and acid were denoted as TOF_{base} and TOF_{acid}, respectively. The calculation results show that Fe−N−C_{NH4I} exhibited a TOF_{base} value of 11.33 e $site^{-1}$ s^{-1} at 0.90 V versus RHE and a TOF_{acid} value of 2.97 e $site^{-1}$ s^{-1} at 0.80 V versus RHE, which are significantly superior to those of Fe−N−C_p (TOF_{base} = 1.46 e $site^{-1}$ s^{-1},

TOF_{acid} = 1.64 e site^{-1} s^{-1}) and Fe−N−C_{NH3} (TOF_{base} = 2.18 e site^{-1} s^{-1}, TOF_{acid} = 1.52 e site^{-1} s^{-1}).

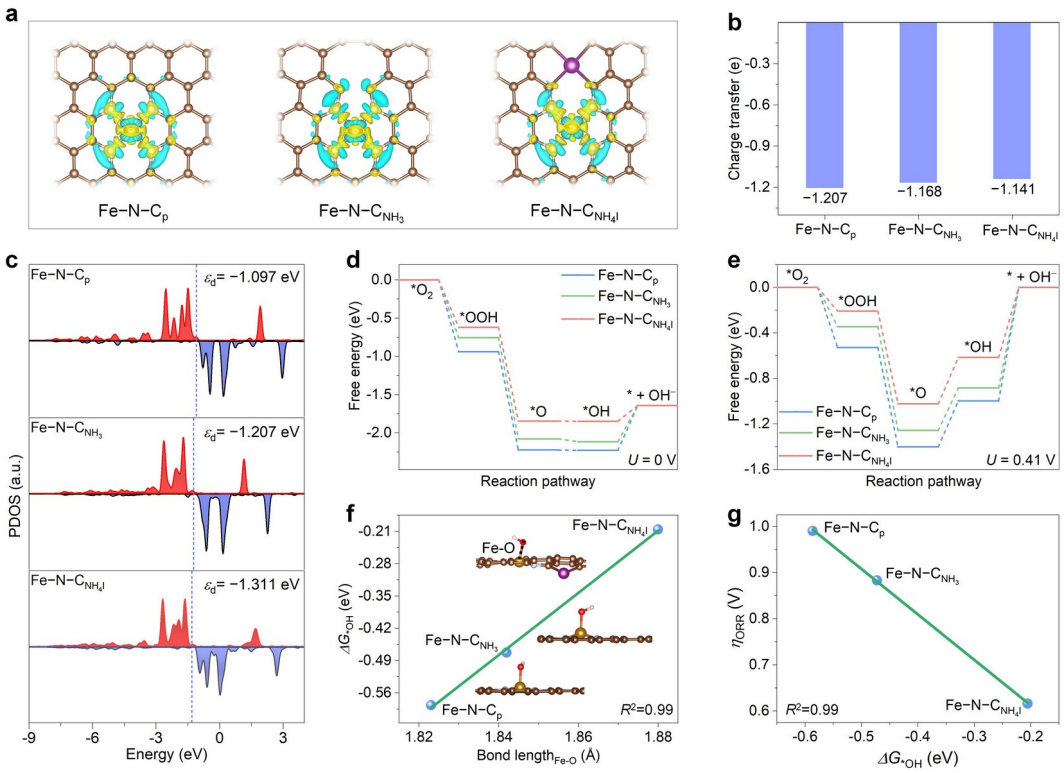

Figure 5. DFT calculations. The charge density difference (a) and the Bader charge analysis (b) of Fe−N−C_p, Fe−N−C_{NH3} and Fe−N−C_{NH4I}. The brown and purple balls represent C and I atoms, respectively. Yellow and cyan iso-surfaces represent charge density accumulation and depletion areas, respectively, with the iso-value of 0.004 electrons Bohr^{-3}. (c) The PDOS of Fe in Fe−N−C_p, Fe−N−C_{NH3} and Fe−N−C_{NH4I}. The Fermi level is set to 0 eV and the *d*-band center (dashed line) is labeled in the diagram. The calculated free-energy diagram of ORR for three atomic structural

329 models at U = 0 V (d) and U = 0.41 V (e) in the alkaline electrolyte. (f) The
330 dependence of ΔG_{*OH} on the bond length of Fe−O and (g) the calculated η_{ORR}. The
331 inset in (f) shows the optimized configurations of *OH adsorbed on Fe−N−C_p,
332 Fe−N−C_{NH3} and Fe−N−C_{NH4I}.

333 **Insights into the enhanced intrinsic activity by DFT calculations.** To elucidate the
334 underlying reason for the improved ORR intrinsic activity of Fe−N−C_{NH4I}, density
335 functional theory (DFT) calculations were conducted. Given the uncertainty in the
336 coordination configuration of the I atom and the relative position between I and Fe,
337 six model catalysts were built (Figure S15 and S16). By using the formation energy
338 and ORR limiting potential as the screening metrics, the moiety with four C-
339 coordinated I atom close to the Fe site was selected to represent Fe−N−C_{NH4I}. In
340 addition, two additional model catalysts, including intact Fe−N_4 configuration and
341 Fe−N_4 with neighboring carbon vacancy, were constructed to represent the control
342 samples of Fe−N−C_p and Fe−N−C_{NH3}, respectively. The optimized structural models
343 for Fe−N−C_{NH4I}, Fe−N−C_p and Fe−N−C_{NH3} were displayed in Figure S17. As shown
344 in the charge density difference distribution plots (Figure 5a), Fe−N−C_p displays a

symmetrical charge distribution around the Fe center, while Fe−N−C_{NH3} and Fe−N−C_{NH4I} undergo symmetry-breaking charge redistributions due to the electronic perturbation by the carbon vacancy and the I dopant, respectively.[52, 53] The degree of charge transfer from Fe to the surrounding environment was found to be different among the three catalysts. Specifically, the number of electrons transferred per Fe atom is fewer for Fe−N−C_{NH4I} (1.141 |*e*|) than Fe−N−C_{NH3} (1.168 |*e*|) and Fe−N−C_p (1.207 |*e*|), giving it a lower Fe oxidation state, in line with the experimental results by XANES and XPS (Figure 2e-g). The projected density of states (PDOS) analysis revealed a negative shift of the *d*-band center for Fe−N−C_{NH4I} (−1.311 eV) compared to Fe−N−C_{NH3} (−1.207 eV) and Fe−N−C_p (−1.097 eV), indicating that the adsorption of the ORR intermediates could be weakened.[54, 55] To confirm this, the adsorption behaviors and the charge density distribution of the catalysts absorbed with different oxygen intermediates were analyzed (Figure S18 and S19). The results show that Fe−N−C_{NH4I} exhibited the lowest degree of electron transfer between Fe and the oxygen intermediates among the three catalysts, suggesting its weakened binding between the Fe site and the reaction intermediates that could facilitate the ORR process.

The Gibbs free energy diagrams of the ORR reaction pathways for the three catalysts at U = 0 V and 0.41 V reveal that the rate-determining step (RDS) of the ORR is the desorption of the *OH intermediates and the theoretical overpotential (η_{ORR}) follows the order of Fe−N−C_{NH4I} (0.62 V) < Fe−N−C_{NH3} (0.88 V) < Fe−N−C_p (1.00 V) (Figure 5d,e and Table S4,S5).[56] Given that *OH is the key intermediate for the RDS, the Fe−O bond length for the OH-adsorbed Fe moiety (i.e., Fe−OH adduct) was calculated for the three catalysts (Table S6). As shown in Figure 5f, the Fe−O bond length shows a linear relationship with the *OH adsorption energy of (ΔG_{*OH}). Among the three catalysts, Fe−N−C_{NH4I} has the largest Fe−O bond length and thus the weakest adsorption strength of *OH.[57] In addition, ΔG_{*OH} is linearly correlated to the calculated η_{ORR} and the experimentally determined $E_{1/2}$ (Figure 5g and Figure S20), suggesting that ΔG_{*OH} is a good descriptor to evaluate the ORR activity of the catalysts. These DFT calculation results suggest that the incorporation of I dopants can rearrange the electron distribution in Fe−N−C_{NH4I} to downshift the *d*-band center and weaken the adsorption of oxygen intermediates to accelerate the 4-electron transfer process, corroborating the experimental findings.

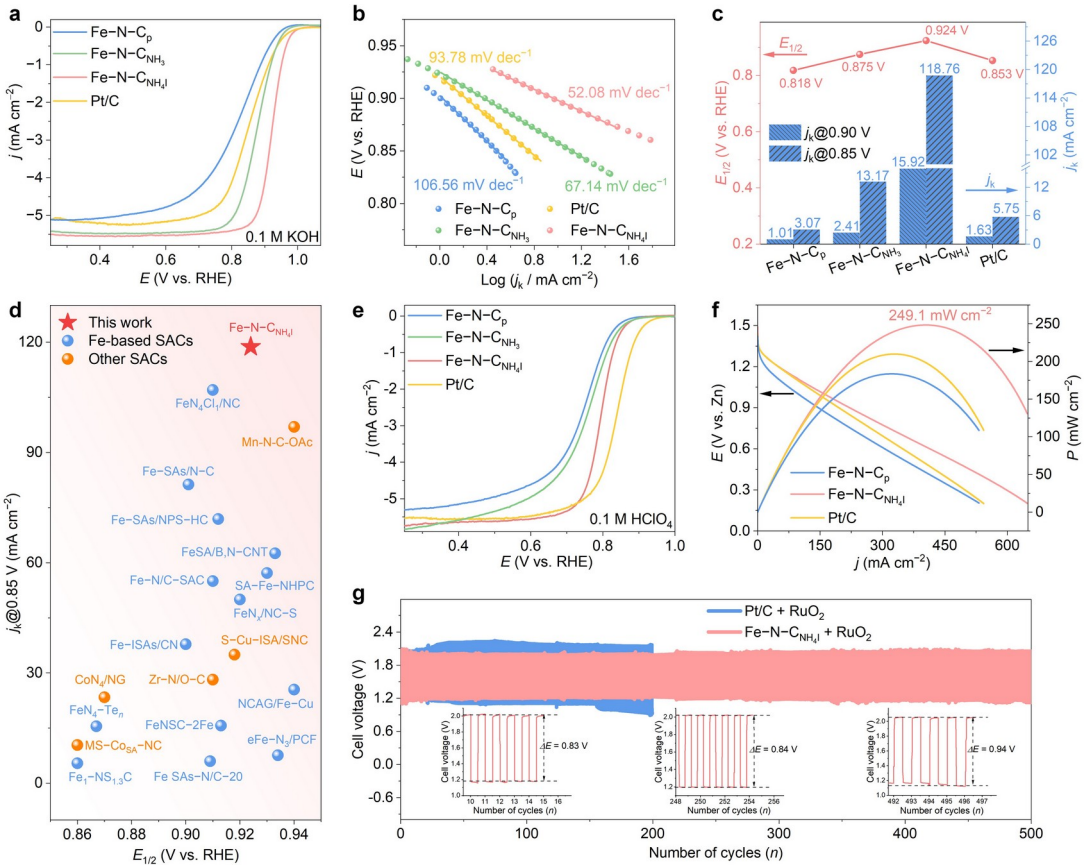

Figure 6. ORR performance and application in Zn-air battery. (a) Polarization curves in 0.1 M KOH for Fe−N−C_{NH4I} and the control samples, along with commercial Pt/C reference. (b) Tafel plots of the corresponding samples in (a). (c) Comparison of $E_{1/2}$ and j_k at 0.90 V and 0.85 V versus RHE for Fe−N−C_{NH4I} and the control samples. (d) Comparison of ORR activities in terms of $E_{1/2}$ and j_k at 0.85 V versus RHE between Fe−N−C_{NH4I} and the state-of-the-art Fe−N−C or other M−N−C reported recently (Table S7). (e) Polarization curves in 0.1 M $HClO_4$ for Fe−N−C_{NH4I} and the control

samples, along with commercial Pt/C reference. (f) The discharge polarization and the corresponding power density curves of Zn-air batteries. (g) The long-term discharge/charge cycling performance of Zn-air batteries with Fe−N−C_{NH4I} and Pt/C as ORR catalyst and RuO_2 as the OER catalyst at a current density of 10 mA cm^{-2} (time constraint = 20 min per cycle). Inset: the voltage gap of the Zn–air battery based on Fe−N−C_{NH4I} + RuO_2 during the cycling test.

ORR performance and application in Zn-air battery. The ORR activity of Fe−N−C_{NH4I} was firstly evaluated in 0.1 M KOH with the rotating disk electrode (RDE). All potentials were converted to the RHE scale based on the calibration results (Figure S21). It is noted that the ORR activity of Fe−N−C_{NH4I} had been optimized by adjusting the amounts of Fe precursors and the temperature of the NH_4I treatment during preparation (Figure S22). From the CV curves, Fe−N−C_{NH4I} exhibited a notable O_2 reduction peak and largest cathodic peak current density compared with control samples (Figure S23). Figure 6a presents the linear sweep voltammetry (LSV) curves with 95% *iR*-compensation of Fe−N−C_{NH4I}, Fe−N−C_{NH3} and Fe−N−C_p, along with the commercial Pt/C for reference purpose. The ORR activity of the catalysts

follows the trend of Fe−N−C_{NH4I} > Fe−N−C_{NH3} > Fe−N−C_p. Specifically, Fe−N−C_{NH4I} has a half-wave potential ($E_{1/2}$) of 0.924 V, much more positive than those of Fe−N−C_{NH3} (0.875 V), Fe−N−C_p (0.818 V) and Pt/C (0.853 V) (Figure 6c). Tafel plots in Figure 6b reveal that Fe−N−C_{NH4I} possesses a much lower Tafel slope of 52.08 mV dec^{-1} compared to Fe−N−C_{NH3} (67.14 mV dec^{-1}), Fe−N−C_p (106.56 mV dec^{-1}) and Pt/C (93.78 mV dec^{-1}). In addition, Fe−N−C_{NH4I} has a kinetic current density (j_k) of 118.76 mA cm^{-2} at 0.85 V and 15.92 mA cm^{-2} at 0.90 V, significantly larger than the control catalysts and the Pt/C reference (Figure 6c). The faster ORR kinetics of Fe−N−C_{NH4I} was further corroborated by electrochemical impedance spectroscopy (EIS) measurements (Figure S24). The electron transfer number (n) for Fe−N−C_{NH4I} derived from rotating ring disk electrode (RRDE) tests fell within the 3.93−3.96 range, in line with Koutecký-Levich (K-L) plot analyses, suggesting the 4-electron ORR process (Figure S25 and S26). When comparing the activity in terms of $E_{1/2}$ and j_k with previously reported ORR catalysts, Fe−N−C_{NH4I} ranks as one of the most

active ORR catalysts (Figure 6d and Table S7). The catalytic stability of Fe−N−C_{NH4I} was evaluated by chronoamperometry technique and CV cycling (Figure S27). The results show that Fe−N−C_{NH4I} displayed a current retention of 96.7% after 11-h continuous electrolysis at a constant potential of 0.80 V and only 12 mV degradation in the value of $E_{1/2}$ after 20000 CV scans, indicating its high durability that is comparable or even superior to recently reported M−N−C catalysts (Table S8). XPS and HAADF-STEM characterizations on the sample collected after stability tests reveal that the atomic Fe dispersion and the I dopants were maintained in Fe−N−C_{NH4I} (Figure S28 and S29). Furthermore, Fe−N−C_{NH4I} revealed excellent methanol resistance with negligible current decay after injecting methanol into the electrolyte (Figure S30). The ORR activity of the catalysts was also evaluated in 0.1 M $HClO_4$. Notably, Fe−N−C_{NH4I} shows a $E_{1/2}$ of 0.795 V, a Tafel slope of 52.8 mV dec^{-1}, and a j_k of 28.57 mA cm^{-2} (at 0.75 V), superior to Fe−N−C_{NH3} and Fe−N−C_p (Figure 6e and Figure S31).

Motivated by the excellent ORR performance of Fe−N−C_{NH4I}, a primary Zn-air battery was assembled with Zn foil as the anode and the carbon paper coated with

Fe−N−C_{NH4I} as the cathode (Figure S32). The as-fabricated Zn-air battery exhibited a high open circuit potential of 1.49 V and an outstanding specific capacity of 822.8 mAh g_{Zn}^{-1}, which were superior to the batteries assembled with Fe−N−C_p and Pt/C (Figure S33). From the discharge polarization curves and the corresponding power density curves in Figure 6f, Fe−N−C_{NH4I} displayed the lowest overpotentials (particularly at high current densities) among all tested samples and it exhibited a peak power density of 249.1 mW cm^{-2}, outperforming Fe−N−C_p (183.5 mW cm^{-2}) and Pt/C (209.8 mW cm^{-2}). In addition, the better rate capability of Fe−N−C_{NH4I} was demonstrated by its higher discharge voltage plateaus compared to control samples and smaller voltage drops when being discharged at various current densities (Figure S34). Then, a rechargeable Zn-air battery was assembled with the composite catalyst of Fe−N−C_{NH4I} + RuO_2 as the cathode. For comparison purpose, another Zn-air battery was assembled with Pt/C + RuO_2 as the cathode. The cycling performances of these two batteries were evaluated by galvanostatic discharge-charge technique (discharge time: 10 min; charge time:10 min) at a constant current density of 10 mA cm^{-2}. As shown in Figure 6g, for Fe−N−C_{NH4I} + RuO_2, the voltage gap between the discharge and charge plateaus was 0.83 V during the initial few cycles and it increased slightly to 0.84 V (10 mV degradation) after ~ 250 cycles and then to 0.94 V (110 mV

degradation) after ~ 500 cycles, demonstrating its excellent cycling stability and reversibility. In comparison, the battery assembled with Pt/C + RuO_2 suffered from much more severe voltage increments within 200 cycles. It is noticeable that the performance of Zn-air battery assembled with Fe−N−C_{NH4I} is superior or comparable to those of the previously reported catalysts (Table S9). Furthermore, XPS and HAADF-STEM characterizations on the cycled Fe−N−C_{NH4I} catalyst suggested that the atomic dispersion and uniform distribution of the Fe and I elements were well maintained (Figure S35 and S36), highlighting the high structural stability of Fe−N−C_{NH4I}.

Conclusion

Numerous heteroatom doping strategies have been developed to optimize the performance of the Fe−N−C catalysts with the focus on the enhancement of the intrinsic activity via the electronic tuning effect. In contrast, results from the current study demonstrated that treating a typical Fe−N−C material with NH_4I vapor via a one-step chemical vapor deposition process could simultaneously increase the SD and TOF values, leading to the development of a highly active Fe−N−C ORR catalyst. The high-temperature NH_4I treatment increased the surface area and porosity of the catalyst via etching the carbon matrix with the in-situ generated NH_3 from the decomposition of NH_4I, resulting in the enhanced exposure of active sites and thus a

high SD value of 2.15×10^{19} sites g^{-1} (×2 enhancement compared to the untreated Fe−N−C catalyst). At the same time, the NH_4I treatment enhanced the intrinsic activity of the Fe−N−C catalyst by I dopants-induced electronic structure tuning that led to the optimization of the adsorption strength of the ORR intermediates, offering a high TOF value of 3.71 electrons $site^{-1}$ s^{-1} (×3 enhancement). As a result, the NH_4I-treated Fe−N−C catalyst performed excellently in both acidic and alkaline electrolytes. Particularly, it exhibited a positive half-wave potential of 0.924 V, a high kinetic current density of 118.76 mA cm^{-2} at 0.85 V and superior power density of 249.1 mW cm^{-2} in a Zn-air battery. Our two-in-one strategy by NH_4I treatment is general to improve the catalytic activity of other types of M−N−C catalysts by simultaneously increasing the surface area/porosity and tuning the electronic structure by I-doping, as demonstrated in the cases of Co−N−C and Mn−N−C (Figure S37, S38 and Table S10). This work provides a facile and efficient strategy to optimize the SD and TOF values of the Fe−N−C catalysts in a concerted manner and can act to guide the rational design and synthesis of highly active PGM-free catalysts for various energy conversion devices.

Supporting Information

Supporting Information is available from the Wiley Online Library or from the author.

Acknowledgment

H.F. acknowledges financial support from the National Natural Science Foundation of China (Grant No. 22479044) and the Innovative Research Groups of Hunan Province

(Grant No. 2020JJ1001). G.Y. acknowledges support from the National Natural Science Foundation of China (Grant No. 22209043). D. W. acknowledges the financial support from the Research Funds of Institute of Zhejiang University-Quzhou (IZQ2021RCZX040, IZQ2023KJ1002). J.L. acknowledges the financial support from the Postdoctoral Fellowship Program of CPSF (Grant No. GZC20240447) and the China Postdoctoral Science Foundation (2024M750860). The authors thank the BL1W1B in the Beijing Synchrotron Radiation Facility (BSRF). We acknowledge the Analytical Instrumentation Center of Hunan University for materials characterizations.

Conflict of Interest

The authors declare no conflict of interest.

Keywords: iron-nitrogen-carbon, turnover frequency, site density, oxygen reduction reaction, ammonium iodide

References

[1] C. Chen, H. Jin, P. Wang, X. Sun, M. Jaroniec, Y. Zheng, S.-Z. Qiao, *Chem. Soc. Rev.* **2024**, *53*, 2022-2055.

[2] X. Wan, J. Shui, *ACS Energy Lett.* **2022**, *7*, 1696-1705.

[3] Z. Miao, S. Li, C. Priest, T. Wang, G. Wu, Q. Li, *Adv. Mater.* **2022**, *34*, 2200595.

[4] J. Li, C. Chen, L. Xu, Y. Zhang, W. Wei, E. Zhao, Y. Wu, C. Chen, *JACS Au* **2023**, *3*, 736-755.

[5] J. Yu, C. Su, L. Shang, T. Zhang, *ACS Nano* **2023**, *17*, 19514-19525.

[6] Y. He, G. Wu, *Acc. Mater. Res.* **2022**, *3*, 224-236.

[7] Y. Zeng, C. Li, B. Li, J. Liang, M. J. Zachman, D. A. Cullen, R. P. Hermann, E. E. Alp, B. Lavina, S. Karakalos, M. Lucero, B. Zhang, M. Wang, Z. Feng, G. Wang, J. Xie, D. J. Myers, J.-P. Dodelet, G. Wu, *Nat. Catal.* **2023**, *6*, 1215-1227.

[8] J. Li, W. Xia, X. Xu, D. Jiang, Z.-X. Cai, J. Tang, Y. Guo, X. Huang, T. Wang, J. He, B. Han, Y. Yamauchi, *J. Am. Chem. Soc.* **2023**, *145*, 27262-27272.

[9] H. Zhang, H.-C. Chen, S. Feizpoor, L. Li, X. Zhang, X. Xu, Z. Zhuang, Z. Li, W. Hu, R. Snyders, D. Wang, C. Wang, *Adv. Mater.* **2024**, *36*, 2400523.

[10] Y. Wang, L. Wang, H. Fu, *Sci. China Mater.* **2022**, *65*, 1701-1722.

[11] N. Ohri, Y. Hua, R. Baidoun, D. Kim, *Chem Catal.* **2023**, *3*, 100837.

[12] E. Luo, Y. Chu, J. Liu, Z. Shi, S. Zhu, L. Gong, J. Ge, C. H. Choi, C. Liu, W. Xing, *Energy Environ. Sci.* **2021**, *14*, 2158-2185.

[13] Y.-F. Guo, S. Zhao, N. Zhang, Z.-L. Liu, P.-F. Wang, J.-H. Zhang, Y. Xie, T.-F. Yi, *Energy Environ. Sci.* **2024**, *17*, 1725-1755.

[14] W. Song, C. Xiao, J. Ding, Z. Huang, X. Yang, T. Zhang, D. Mitlin, W. Hu, *Adv. Mater.* **2024**, *36*, 2301477.

[15] F. Luo, S. Wagner, W. Ju, M. Primbs, S. Li, H. Wang, U. I. Kramm, P. Strasser, *J. Am. Chem. Soc.* **2022**, *144*, 13487-13498.

[16] Z. Jin, P. Li, Z. Fang, G. Yu, *Acc. Chem. Res.* **2022**, *55*, 759-769.

[17] M. Primbs, Y. Sun, A. Roy, D. Malko, A. Mehmood, M.-T. Sougrati, P.-Y. Blanchard, G. Granozzi, T. Kosmala, G. Daniel, P. Atanassov, J. Sharman, C. Durante, A. Kucernak, D. Jones, F. Jaouen, P. Strasser, *Energy Environ. Sci.* **2020**, *13*, 2480-2500.

[18] M. Tang, T. Yang, X. Wang, J. Ge, *J. Phys. Chem. C* **2024**, *128*, 1547-1561.

[19] Y. Zhang, S. Zhu, X. Wang, Z. Jin, J. Ge, C. Liu, W. Xing, *J Electroanal. Chem.* **2023**, *943*, 117506.

[20] Y. Wu, Z. Zhuang, C. Chen, J. Li, F. Xiao, C. Chen, *Chem Catal.* **2023**, *3*, 10065.

[21] Y. Li, S. Yin, L. Chen, X. Cheng, C. Wang, Y. Jiang, S. Sun, *Energy Environ. Mater.* **2024**, *7*, e12611.

[22] L. Jiao, J. Li, L. L. Richard, Q. Sun, T. Stracensky, E. Liu, M. T. Sougrati, Z. Zhao, F. Yang, S. Zhong, H. Xu, S. Mukerjee, Y. Huang, D. A. Cullen, J. H. Park, M. Ferrandon, D. J. Myers, F. Jaouen, Q. Jia, *Nat. Mater.* **2021**, *20*, 1385-1391.

[23] J. Wu, L. Xiong, B. Zhao, M. Liu, L. Huang, *Small Methods* **2020**, *4*, 1900540.

[24] C. Xia, Y. Qiu, Y. Xia, P. Zhu, G. King, X. Zhang, Z. Wu, J. Y. Kim, D. A. Cullen, D. Zheng, P. Li, M. Shakouri, E. Heredia, P. Cui, H. N. Alshareef, Y. Hu, H. Wang, *Nat. Chem.* **2021**, *13*, 887-894.

[25] J. Wang, Z. Li, Y. Wu, Y. Li, *Adv. Mater.* **2018**, *30*, 1801649.

[26] A. Mehmood, M. Gong, F. Jaouen, A. Roy, A. Zitolo, A. Khan, M.-T. Sougrati, M. Primbs, A. M. Bonastre, D. Fongalland, G. Drazic, P. Strasser, A. Kucernak, *Nat. Catal.* **2022**, *5*, 311-323.

[27] X. Wan, X. Liu, Y. Li, R. Yu, L. Zheng, W. Yan, H. Wang, M. Xu, J. Shui, *Nat. Catal.* **2019**, *2*, 259-268.

[28] H. Zhang, S. Hwang, M. Wang, Z. Feng, S. Karakalos, L. Luo, Z. Qiao, X. Xie, C. Wang, D. Su, Y. Shao, G. Wu, *J. Am. Chem. Soc.* **2017**, *139*, 14143-14149.

[29] H. Zhang, H. T. Chung, D. A. Cullen, S. Wagner, U. I. Kramm, K. L. More, P. Zelenay, G. Wu, *Energy Environ. Sci.* **2019**, *12*, 2548-2558.

[30] J. Zhu, X. F. Lu, D. Luan, X. W. Lou, *Angew. Chem. Int. Ed.* **2024**, *63*,

559 e202408846.
560 [31] Z. Wang, Z. Lu, Q. Ye, Z. Yang, R. Xu, K. Kong, Y. Zhang, T. Yan, Y. Liu, Z.
561 Pan, Y. Huang, X. Lu, *Adv. Funct. Mater.* **2024**, *34*, 2315150.
562 [32] H. Fei, J. Dong, Y. Feng, C. S. Allen, C. Wan, B. Volosskiy, M. Li, Z. Zhao, Y.
563 Wang, H. Sun, P. An, W. Chen, Z. Guo, C. Lee, D. Chen, I. Shakir, M. Liu, T. Hu, Y.
564 Li, A. I. Kirkland, X. Duan, Y. Huang, *Nat. Catal.* **2018**, *1*, 63-72.
565 [33] Y. Zeng, C. Li, B. Li, J. Liang, M. J. Zachman, D. A. Cullen, R. P. Hermann, E.
566 E. Alp, B. Lavina, S. Karakalos, M. Lucero, B. Zhang, M. Wang, Z. Feng, G. Wang, J.
567 Xie, D. J. Myers, J.-P. Dodelet, G. Wu, *Nat. Catal.* **2023**, *6*, 1215-1227.
568 [34] S. Yin, L. Chen, J. Yang, X. Cheng, H. Zeng, Y. Hong, H. Huang, X. Kuai, Y.
569 Lin, R. Huang, Y. Jiang, S. Sun, *Nat. Commun.* **2024**, *15*, 7489.
570 [35] Y. Pan, X. Ma, M. Wang, X. Yang, S. Liu, H.-C. Chen, Z. Zhuang, Y. Zhang, W.-
571 C. Cheong, C. Zhang, X. Cao, R. Shen, Q. Xu, W. Zhu, Y. Liu, X. Wang, X. Zhang,
572 W. Yan, J. Li, H. M. Chen, C. Chen, Y. Li, *Adv. Mater.* **2022**, *34*, 2203621.
573 [36] J. Liu, D. Wang, K. Huang, J. Dong, J. Liao, S. Dai, X. Tang, M. Yan, H. Gong,
574 J. Liu, Z. Gong, R. Liu, C. Cui, G. Ye, X. Zou, H. Fei, *ACS Nano* **2021**, *15*, 18125-
575 18134.
576 [37] M. L. Schlegel, P. Reiller, F. Mercier-Bion, N. Barré, V. Moulin, *Geochim.*
577 *Cosmochim. Acta* **2006**, *70*, 5536-5551.
578 [38] J. Zhou, M. L. Holekevi Chandrappa, S. Tan, S. Wang, C. Wu, H. Nguyen, C.
579 Wang, H. Liu, S. Yu, Q. R. S. Miller, G. Hyun, J. Holoubek, J. Hong, Y. Xiao, C.
580 Soulen, Z. Fan, E. E. Fullerton, C. J. Brooks, C. Wang, R. J. Clément, Y. Yao, E. Hu,

S. P. Ong, P. Liu, *Nature* **2024**, *627*, 301-305.

[39] L. Hu, C. Dai, L. Chen, Y. Zhu, Y. Hao, Q. Zhang, L. Gu, X. Feng, S. Yuan, L. Wang, B. Wang, *Angew. Chem. Int. Ed.* **2021**, *60*, 27324-27329.

[40] Y. Ren, Z. Ma, R. E. Morris, Z. Liu, F. Jiao, S. Dai, P. G. Bruce, *Nat. Commun.* **2013**, *4*, 2015.

[41] Q. Wang, Y. Yang, F. Sun, G. Chen, J. Wang, L. Peng, W.-T. Chen, L. Shang, J. Zhao, D. Sun-Waterhouse, T. Zhang, G. I. N. Waterhouse, *Adv. Energy Mater.* **2021**, *11*, 2100219.

[42] F. Jaouen, M. Lefèvre, J.-P. Dodelet, M. Cai, *J. Phys. Chem. B* **2006**, *110*, 5553-5558.

[43] Y. Dong, Q. Zhang, Z. Tian, B. Li, W. Yan, S. Wang, K. Jiang, J. Su, C. W. Oloman, E. L. Gyenge, R. Ge, Z. Lu, X. Ji, L. Chen, *Adv. Mater.* **2020**, *32*, 2001300.

[44] Y. Zhan, H. Zeng, T. Zhao, A. Situ, L. Yang, Z. Zhang, P. Li, Z. Wang, J. Wen, F. Xie, J. Chen, X. Tang, H. Meng, *Int. J. Hydrogen Energy* **2024**, *56*, 1049-1056.

[45] S. Y. Yi, E. Choi, H. Y. Jang, S. Lee, J. Park, D. Choi, Y. Jang, H. Kang, S. Back, S. Jang, J. Lee, *Adv. Mater.* **2023**, *35*, 2302666.

[46] M. Du, B. Chu, Q. Wang, C. Li, Y. Lu, Z. Zhang, X. Xiao, C.-Q. Xu, M. Gu, J. Li, H. Pang, Q. Xu, *Adv. Mater.* **2024**, *36*, 2412978.

[47] K.-M. Zhao, S. Liu, Y.-Y. Li, X. Wei, G. Ye, W. Zhu, Y. Su, J. Wang, H. Liu, Z. He, Z.-Y. Zhou, S.-G. Sun, *Adv. Energy Mater.* **2022**, *12*, 2103588.

[48] X. Wang, Z.-Y. Yi, Y.-Q. Wang, D. Wang, *Angew. Chem. Int. Ed.* **2024**, e202413673.

[49] S. Zhang, X. Liu, Z. Li, L. Hao, P. Wang, X. Zou, Z. Liu, G. Zhang, C.-Y. Zhang,

ACS Sustainable Chem. Eng. **2019**, *7*, 11787-11794.

[50] D. Malko, A. Kucernak, T. Lopes, *Nat. Commun.* **2016**, *7*, 13285.

[51] S.-H. Yin, S.-L. Yang, G. Li, G. Li, B.-W. Zhang, C.-T. Wang, M.-S. Chen, H.-G. Liao, J. Yang, Y.-X. Jiang, S.-G. Sun, *Energy Environ. Sci.* **2022**, *15*, 3033-3040.

[52] S. Wei, R. Yang, Z. Wang, J. Zhang, X.-H. Bu, *Adv. Mater.* **2024**, 2404692.

[53] H. Liu, L. Jiang, Y. Sun, J. Khan, B. Feng, J. Xiao, H. Zhang, H. Xie, L. Li, S. Wang, L. Han, *Adv. Funct. Mater.* **2023**, *33*, 2304074.

[54] L. Peng, J. Yang, Y. Yang, F. Qian, Q. Wang, D. Sun-Waterhouse, L. Shang, T. Zhang, G. I. N. Waterhouse, *Adv. Mater.* **2022**, *34*, 2202544.

[55] Z. Pei, H. Zhang, Y. Guo, D. Luan, X. Gu, X. W. Lou, *Adv. Mater.* **2024**, *36*, 2306047.

[56] P. Zhang, H.-C. Chen, H. Zhu, K. Chen, T. Li, Y. Zhao, J. Li, R. Hu, S. Huang, W. Zhu, Y. Liu, Y. Pan, *Nat. Commun.* **2024**, *15*, 2062.

[57] H. Huang, D. Yu, F. Hu, S.-C. Huang, J. Song, H.-Y. Chen, L. L. Li, S. Peng, *Angew. Chem. Int. Ed.* **2022**, *61*, e202116068.

ToC figure

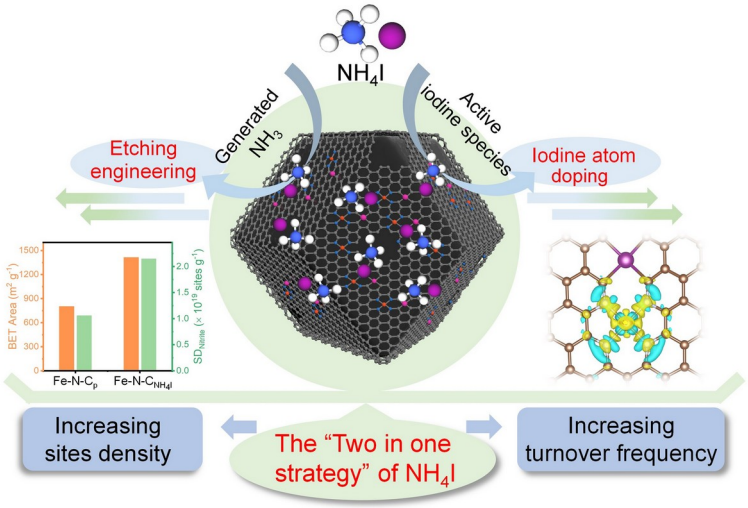

Treating a Fe−N−C catalyst with NH_4I vapor via a one-step chemical vapor deposition process leads to the simultaneous improvements in the turnover frequency via the I-doping induced electronic structure tuning and site density via the etching of carbon substrate by the in-situ generated NH_3, resulting in superior oxygen reduction activity in both acidic and alkaline media.